Energetics and Mechanism of Ca^{2+} Displacement by Lanthanides in a Calcium Binding Protein†

Sourajit M. Mustafi,‡ Sulakshana Mukherjee,‡ Kandala V. R. Chary,*,‡ Cristina Del Bianco,§ and Claudio Luchinat§

Department of Chemical Sciences, Tata Institute of Fundamental Research, Mumbai 400 005, India, and Centro Risonanze Magnetiche, University of Florence, Florence, Italy

Received February 15, 2004; Revised Manuscript Received May 22, 2004

ABSTRACT: The displacement of Ca^{2+} by trivalent lanthanide ions (Tm^{3+}) in a protozoan (*Entamoeba histolytica*) Ca^{2+} binding protein has been studied by NMR and isothermal calorimetry (ITC). The study provides a basis for understanding the behavior of lanthanides when used as a substitute for Ca^{2+}, the pattern of sequential binding, the structural changes involved, the range and magnitude of paramagnetic interaction, and the associated energetics and mechanism. The progressive Ca^{2+} displacement from site III first, followed by displacement from site II, I, and IV, as observed during the NMR titration experiments, is interpreted in the light of ITC data to provide a deeper insight into the intradomain and, for the first time, interdomain cooperativity and information about the statistical phenomenon involved in it. A theoretical model governing Ca^{2+} displacement is provided. The small structural changes involved in Ca^{2+} displacement by a diamagnetic lanthanide (La^{3+}) has also been monitored.

Entamoeba histolytica, a protozoan parasite, is the causative agent of amoebiasis and amoebic dysentery worldwide (*1*). Calcium is thought to be involved in the pathogenetic mechanisms of amoebiasis (*2*−*4*). One of the calcium binding proteins from this organism (hereafter refer to as *Eh*CaBP[1]) (*5*) shows homology with other calcium binding proteins in the calcium binding loops but not in the interloop regions, which are suspected to be the sites that interact with other proteins. *Eh*CaBP is a 134 amino acid residue long EF-hand protein (*6*−*11*) ($M_r \approx 14.7$ kDa). The three-dimensional (3D) structure of this protein in its holo form determined earlier (*12*; PDB ID 1JFK) consists of two globular domains connected by a flexible linker region containing eight residues. No nuclear Overhauser effects (NOEs) were observed between the two domains, and the orientation of the two domains with respect to each other is not defined. To obtain information about interdomain orientation, a number of 2D and 3D heteronuclear experiments were carried out on *Eh*CaBP by displacing calcium with paramagnetic metal ions. Lanthanide ions (Ln^{3+}), which have ionic radii (0.85−1.1 Å) similar to those of calcium (0.90 Å), can displace Ca^{2+} in such proteins (*13*, *14*). The paramagnetic Ln^{3+} ions possess large anisotropic magnetic susceptibilities, which result in large pseudocontact shifts (PCSs) of nuclear spins as far as 45 Å from the paramagnetic ion (*14*, *15*) and aid in structure refinement of proteins by providing long-range distance constraints (*15*). Besides, these PCSs can be used to determine the interdomain orientation in multidomain proteins. Residual dipolar couplings that arise due to the partial alignment of proteins containing Ln^{3+} in high magnetic field can be used as further refinement tools (*16*, *17*). Earlier, we carried out Yb^{3+}-substitution studies by NMR and calorimetry (*18*). Yb^{3+} was chosen for the study because of its favorable pseudocontact shift to Curie line-broadening ratio (*19*). Isothermal titration calorimetry (ITC) was used to obtain binding affinities and free energy changes upon substitution of Ca^{2+} by Yb^{3+} and to have an insight of the relative binding specificities and affinities. The titration experiments revealed that Yb^{3+} displaces Ca^{2+} preferentially from site III, and then from sites II and I in the N-terminal domain. Ca^{2+} is finally displaced from site IV only to an extent of 70% of the original population. In this paper, we present a combined NMR and ITC study of Ca^{2+} displacement by thulium (Tm^{3+}) in *Eh*CaBP providing a deeper insight into the intradomain and, for the first time, interdomain cooperativity, as well as into the microscopic pathway involved in displacement of Ca^{2+} by Ln^{3+}.

MATERIALS AND METHODS

Protein Sample Preparation. The protocol described earlier (*12*, *20*) was used for the overexpression of *Eh*CaBP in a minimal (M9) medium and its purification. In the present study, three samples of $(Ca^{2+})_4$-*Eh*CaBP were prepared: (i) uniformly ^{15}N-labeled (u-^{15}N), (ii) arginine, isoleucine, leucine, lysine, and phenylalanine [RILKF] unlabeled and the remaining amino acid residues ^{15}N-labeled, and (iii) uniformly doubly (^{13}C and ^{15}N)-labeled $(Ca^{2+})_4$-*Eh*CaBP. Unknown excess concentration of Ca^{2+} in the protein sample

† This work is supported under an Indo-Italian Joint Research Project, supported by the DST, New Delhi, India and supported by the EC contract No. HPRI-CT-1999-50006 (Transient NMR) and by CNR, Progetto Finalizzato Biotecnologie, 99.XX.

* Author for correspondence. Mailing address: Department of Chemical Sciences, Tata Institute of Fundamental Research, Homi Bhabha Road, Colaba, Mumbai-400005, India. Phone: +0091-22-2280 4545, extension 2489. Fax: 0091-22-2280 4810. E-mail: chary@tifr.res.in.

§ University of Florence.

‡ Tata Institute of Fundamental Research.

[1] Abbreviations: NMR, nuclear magnetic resonance; ITC, isothermal calorimetry; HSQC, heteronuclear single quantum correlation; *Eh*CaBP, *Entamoeba histolytica* calcium binding protein.

10.1021/bi049657d CCC: $27.50
Published on Web 07/02/2004

Scheme 1

```
          1     6     12
MAEALFKEIDVNGDGAVSYEEVKAFVSKKRAIKNEQ
LLQLIFKSIDADGNGEIDQNEFAKFYGSIQGQDLSDDKI
GLKVLYKLMDVDGDGKLTKEEVTSFFKKHGIE
KVAEQVMKADANGDGYITLEEFLEFSL
```

was removed using a 3 kDa cutoff Amicon centricon unit by washing the protein solution first with deionized water and then with 0.1 M KCl solution containing 10% ^2H_2O at pH 6.0 and finally concentrating to 0.6 mL for NMR studies. $CaCl_2$ (20 mM) was added to the concentrated protein sample so that the Ca^{2+} concentration is almost constant and the reaction follows as a pseudo-first-order reaction. The above condition simplifies the analysis. The protein concentrations were estimated using the absorbance at 280 nm ($\epsilon_{280} = 5120$ M^{-1} cm^{-1}) on a Varian Inc. Cary 50 scan spectrophotometer. NMR experiments were performed at 35 °C on 0.6 mL of ~1 mM protein samples (pH 6.0) in a mixed solvent of 90% H_2O and 10% ^2H_2O.

NMR Experiments. NMR experiments were recorded on a Bruker Avance 700 MHz NMR spectrometer (CERM, Florence), Bruker Avance WB 500 MHz NMR spectrometer (NFMR, Mumbai), or Varian Unity$^+$ 600 MHz NMR spectrometer (NFMR, Mumbai), all equipped with pulsed field gradient units and triple resonance probes with actively shielded *Z*-gradients. Sensitivity-enhanced 2D [^{15}N-^{1}H] heteronuclear single quantum coherence (HSQC) spectra using pulsed field gradients for coherence selection (*21*) were recorded during each step of the titration. During the course of titration, samples were found to be stable and soluble. Experiments with uniformly doubly labeled protein include sensitivity-enhanced 2D (^{15}N-^{1}H) HSQC, HNCO (*22*), CBCA-(C0)NH (*23*), CBCANH (*24*), and HN(CA)CO (*25*). Data transformation and processing were done on a Silicon Graphics workstation (R10000 based Indigo II Solid Impact Graphics) using the Felix 97 software (MSI). ^{1}H chemical shifts were calibrated relative to 2,2-dimethyl-2-silapentane-5-sulfonate (DSS) at 308 K (0.0 ppm). ^{13}C chemical shifts were calibrated indirectly, relative to DSS. ^{15}N chemical shifts were calibrated with respect to an external standard of $^{15}NH_4Cl$ (2.9 M in 1 M HCl). The ^{1}H and ^{15}N chemical shifts published earlier (*12*, *20*) were used to identify individual cross-peaks in the [^{15}N-^{1}H] HSQC spectrum.

Tm^{3+}/La^{3+} Titration of $(Ca^{2+})_4$-EhCaBP: The displacement of Ca^{2+} in the protein by paramagnetic Tm^{3+} and diamagnetic La^{3+} was achieved by adding small aliquots from a 20 mM stock solution of $TmCl_3$ to the protein solution. To start, an aliquot of $TmCl_3/LaCl_3$ from a 0.02 M stock solution corresponding to a metal/protein (M/P) ratio of 0.1 was taken each time and added directly to the protein solution in the NMR sample tube. The sample was mixed thoroughly before transferring it to 500, 600, or 700 MHz magnet. For Tm^{3+}, the [^{15}N-^{1}H]-HSQC spectral peaks started broadening out at a M/P ratio of 3.0. Hence, we did not go beyond this ratio. This resulted in a total number of 30 titration points. In the case of La^{3+}, our interest was confined to monitoring structural changes, if any, when the M/P ratio is less than or equal to 1 and hence the titration with $LaCl_3$ was carried

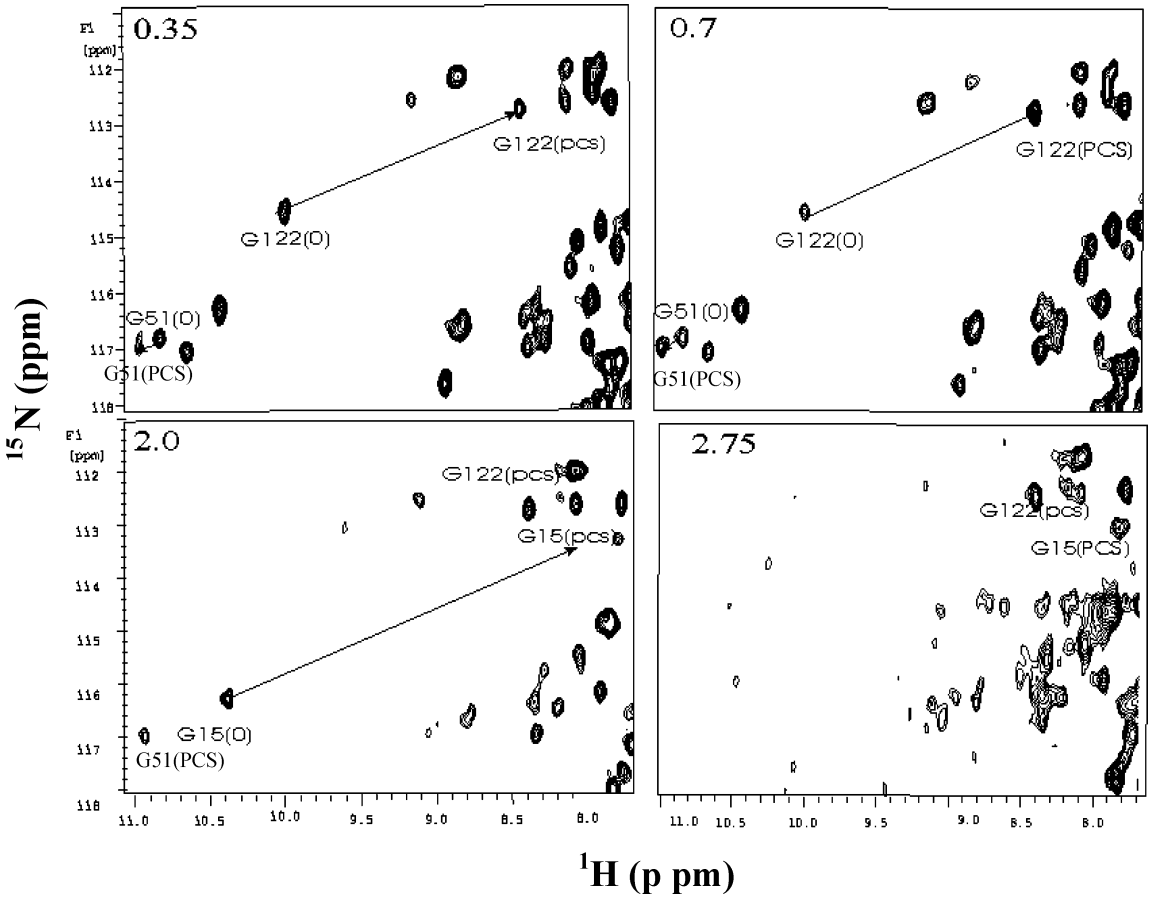

FIGURE 1: Selected regions of the 2D [^{15}N-^{1}H] HSQC spectrum of *Eh*CaBP showing G15, G51, G90, and G122 peaks at different metal/protein ratios. The metal/protein ratio is indicated at top left in panels A−D.

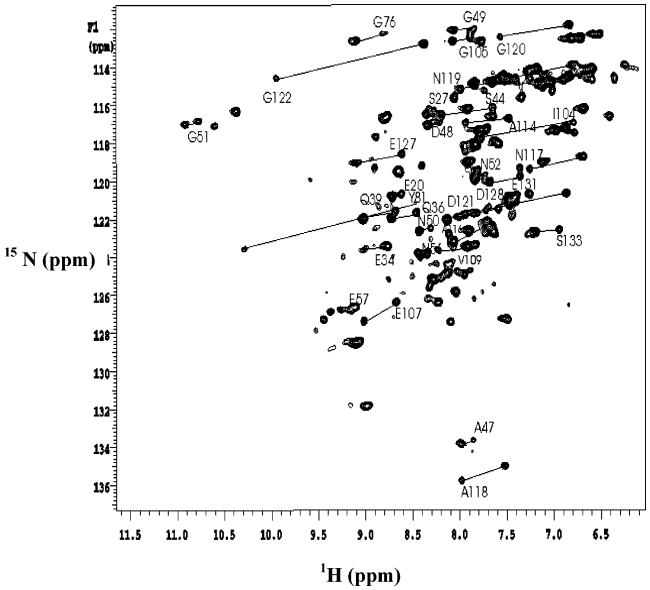

FIGURE 2: 2D [^{15}N-^{1}H] HSQC spectrum of [RILFK]-^{15}N sample with assignments. The arrows point to the appearance of pseudocontact-shifted peaks.

out up to a M/P ratio of 1:1. The change in pH on addition of the lanthanide salts was negligible.

ITC Measurements and Analyses. ITC measurements were performed with a Microcal Omega titration calorimeter. Samples were centrifuged and degassed prior to the titration and examined for precipitation after the titration. A typical titration consisted of injecting 4 μL aliquots of 7.5 mM $TmCl_3$ solution into 0.11 mM (1.3 mL) protein solution every 3 min to ensure that the titration peak returned to the baseline prior to the next injection. A total of 31 injections were carried out. No precipitation was observed during the titration. Aliquots of more concentrated ligand solution were injected into the buffer solution (without the protein) in a separate ITC run to subtract the heat of dilution. All experiments were repeated at least twice. The ITC data were analyzed using software ORIGIN (supplied with the Omega Micro calorimeter). The amount of heat released per addition of the titrating agent was fitted into a macroscopic four sequential binding sites model (*26*).

RESULTS AND DISCUSSION

Tm^{3+} Titration of $(Ca^{2+})_4$-EhCaBP. The amide ($^{1}H^{N}$) protons of the glycine residues at the 6th positions of the four homologous Ca^{2+} binding loops (shown with an underline in Scheme 1), exhibit a characteristic downfield shift in the Ca^{2+}-bound state (*holo*) (*27*). This is due to their involvement in hydrogen bonding with the side-chain carboxyl oxygen of an invariant aspartate at the 1st position (shown as bold letters in Scheme 1).

In *Eh*CaBP, the corresponding glycine residues, G15, G51, G90, and G122, have their $^{1}H^{N}$ chemical shifts at 10.37, 10.75, 10.51, and 9.92 ppm, respectively, and appear in the least crowded region of the spectrum ($\omega_1 = 108.00-115.00$ ppm and $\omega_2 = 9.50-11.00$ ppm). These Gly6 were used as markers to monitor the Ca^{2+} displacement reactions. In the following discussion, the four Ca^{2+}-binding sites present in *Eh*CaBP will be identified as follows: (i) site I (residues 1−32), (ii) site II (residues 33−62), (iii) site III (residues 71−103), and (iv) site IV (residues 104−134).

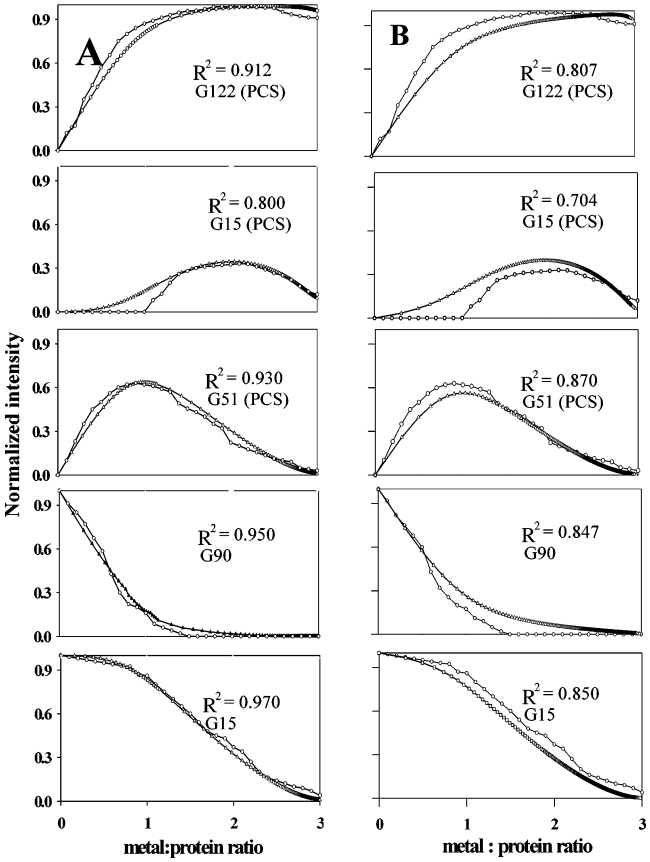

FIGURE 3: Superposition of experimental and simulated plots of intensity profiles of the original peaks of G15 and G90 and pseudocontact-shifted cross-peaks of G15, G51, and G122 during the Tm^{3+} titration by considering the (A) sequential filling model and (B) domain-independent model: (●) simulated curves; (△) experimental curves. The thermodynamic constants used in simulations are listed in Table 1. The corresponding R^2 values are given at the upper-right corner of respective plots.

Titration of [u-^{15}N]-labeled and RILKF-unlabeled *Eh*CaBP was carried out with Tm^{3+}, and changes in the [^{15}N-^{1}H] HSQC spectrum were monitored. During the initial course of titration, several new signals appeared due to pseudocontact shifts. Some of the original peaks showed Curie broadening induced by paramagnetic Tm^{3+}, while others remained unaffected.

Titration up to a Tm^{3+}/EhCaBP Ratio of 1:1. During the titration up to a M/P ratio of 1:1, there is a gradual disappearance of original cross-peaks belonging to sites II, III, and IV and concomitant appearance of new pseudocontact-shifted cross-peaks from sites II and IV. The cross-peaks from site I are virtually unaffected. Figure 1 shows selected regions of the [^{15}N-^{1}H] HSQC spectrum. Selective unlabeling (*28*, *29*) of arginine, isoleucine, leucine, lysine, and phenylalanine results in a dramatic simplification of the HSQC spectrum (Figure 2), which aids in unambiguous resonance assignments of the pseudocontact-shifted peaks, particularly those of residues belonging to sites II and IV. Such assignments were verified using FANTASIA (*30*). For this purpose, with the known structure of the C-terminal domain in hand (PDB ID 1JFK), unambiguously assigned pseudocontact shifts (PCSs) belonging to the C-terminal domain were used to calculate the anisotropy tensors using FANTASIA. This helps to predict unassigned PCSs and match them with the experimental values. Thus, we could assign

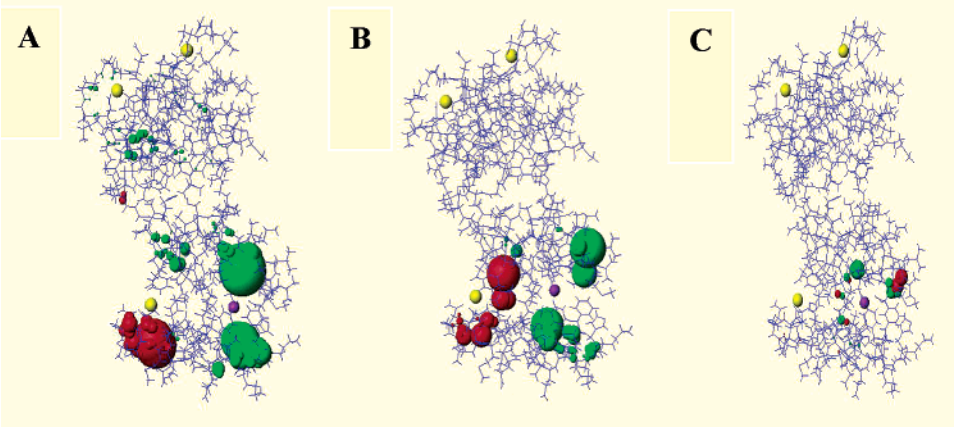

FIGURE 4: Various pseudocontact shifts seen in the [^{15}N-^{1}H]-HSQC spectra of (A) (Tm^{3+})(Ca^{2+})$_3$-*Eh*CaBP and (B) (Yb^{3+})(Ca^{2+})$_3$-*Eh*CaBP and (C) diamagnetic shifts seen in the [^{15}N-^{1}H]-HSQC spectrum of (La^{3+})(Ca^{2+})$_3$-*Eh*CaBP, depicted as spheres using MOLMOL. The red spheres represent the negative shifts, while green ones are positive shifts. The radii of the spheres are proportional to the magnitude of the observed shifts. The shifts seen in the N-terminal domain indicate a higher range of paramagnetic interaction in the case of Tm^{3+}.

70 PCSs for $^{1}H^{N}$ and ^{15}N spins. The corresponding PCS values are small in the N-terminal domain residues.

Figure 3 shows the normalized volumes of cross-peaks plotted for a few amino acid residues in the metal binding sites of *Eh*CaBP. These plots indicate the percentage of various species present at different M/P ratios and reveal that at first Tm^{3+} ions bind predominantly to site III, resulting in almost complete loss of cross-peaks for residues belonging to this site. New pseudocontact-shifted peaks are observed for residues in sites II and IV. Thus, as the titration approaches a M/P ratio of 1:1, site III is almost filled by the Tm^{3+} ions, and the predominant species becomes (Ca^{2+})-(I)-(Ca^{2+})(II)-(Tm^{3+})(III)-(Ca^{2+})(IV)-*Eh*CaBP. The NH groups giving pseudocontact shifts in the HSQC spectra of (Tm^{3+})-(Ca^{2+})$_3$-*Eh*CaBP are depicted in Figure 4A. Three-dimensional (3D) triple resonance spectra recorded with the doubly labeled (Tm^{3+})(Ca^{2+})$_3$-*Eh*CaBP were used in the assignment of pseudocontact shifts for the individual $^{13}C^{\alpha}$, $^{13}C^{\beta}$, and $^{13}C'$ spins in the protein. Figure 5 shows the histograms of differences seen in $^{1}H^{N}$, ^{15}N, $^{13}C^{\alpha}$,$^{13}C^{\beta}$, and $^{13}C'$ chemical shifts for each amino acid residue of (Tm^{3+})(Ca^{2+})$_3$-*Eh*CaBP and (Ca^{2+})$_4$-*Eh*CaBP (values are given in the Supporting Information).

During Yb^{3+} titration (*18*), integral volume of peak G51 decreased by 10−15% from its original value at M/P ratio of 1:1, while that of G90 decreased by 80%, but no interdomain PCSs were seen (Figure 4B). Hence, it could not be inferred whether it was sequential or parallel displacement of Ca^{2+} from sites II and III (*18*). The displacement from the individual domains was thus considered to be independent of each other with no interdomain cooperativity. In the present study, we use Tm^{3+}, which may produce interdomain PCSs by virtue of its higher ligand field and thus may allow us to monitor possible cooperative effects. Tm^{3+} bound in site III indeed produces PCSs in sites II and IV. No species are seen in which Ca^{2+} is first displaced from sites II or IV, which would have produced PCSs in site III. Residues at site I also showed no decrease in their integral volume during this initial course of titration, clearly showing negligible parallel displacement from site I along with site III.

Titration from M/P Ratio of 1:1 to 3:1. At a M/P ratio of 1:1, site III is almost completely substituted by Tm^{3+}. The additional Tm^{3+} can displace Ca^{2+} in sites I, II, and IV.

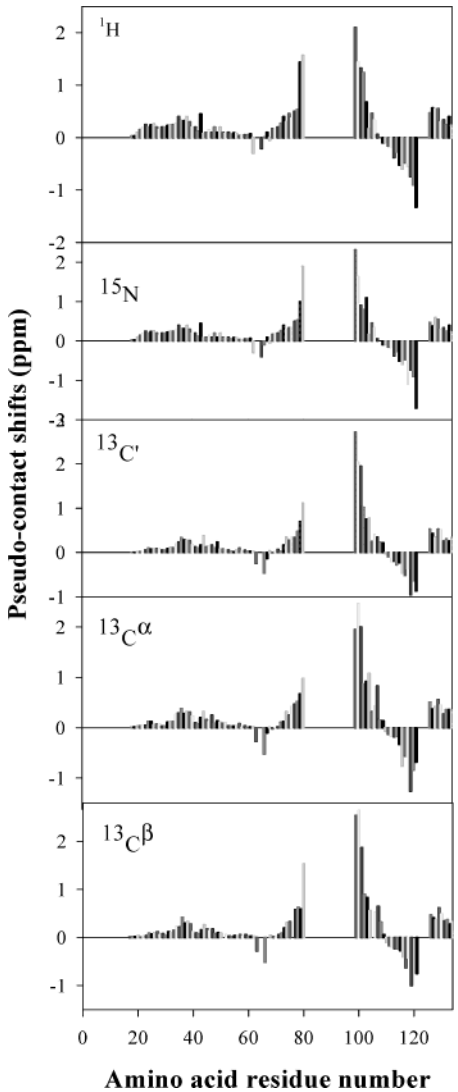

FIGURE 5: The histograms of differences seen in ^{1}H, ^{15}N, $^{13}C^{\alpha}$, $^{13}C^{\beta}$, and $^{13}C'$ chemical shifts for each amino acid residue of (Tm^{3+})(Ca^{2+})$_3$-*Eh*CaBP and (Ca^{2+})$_4$-*Eh*CaBP.

During this stage of titration, one observes (i) gradual and simultaneous disappearance of the original cross-peaks belonging to site I and the pseudocontact-shifted peaks belonging to site II and (ii) appearance of new pseudocontact-

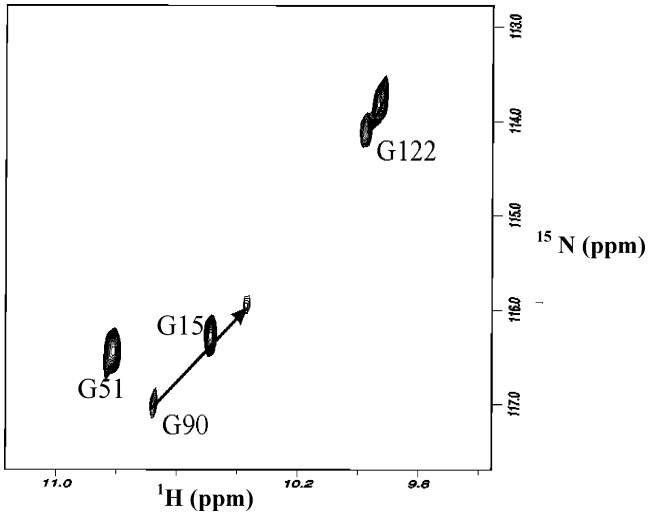

FIGURE 6: Selected regions of the 2D [^{15}N-^{1}H] HSQC spectrum of $(La^{3+})(Ca^{2+})_3$-*Eh*CaBP showing G15, G51, G90, and G122 peaks at a metal/protein ratio of 0.7. The arrows point to the appearance of diamagnetic shifted peaks.

shifted peaks for residues belonging to site I. Panels C and D of Figure 1 show selected regions of the HSQC spectrum, at a M/P ratio of 2.0 and 2.75, respectively. The pseudocontact-shifted peaks due to G51 disappear almost completely as the titration approaches a M/P ratio of 3.0. New pseudocontact-shifted cross-peaks of residues belonging to site I are observed which, later, start disappearing. For example, Figure 1C shows the pseudocontact-shifted cross-peak at $\omega_1 = 113.0$, $\omega_2 = 7.77$ ppm, which is assigned to G15. Furthermore, Figure 3 shows the normalized volumes of cross-peaks for G15 (both original and pseudocontact-shifted peaks) and G51 (pseudocontact-shifted). These plots show that up to a M/P ratio of 3:1, there is a gradual decrease in the volume of cross-peaks of site I and pseudocontact-shifted peaks of site II, while the new pseudocontact-shifted cross-peaks for residues in site I gradually increase in volume up to a M/P ratio of about 2 (Figure 3). Beyond this point, there is gradual fall in their volumes as well. At a M/P ratio of 3:1, species corresponding to Ca^{2+}-bound sites I and II are decreased to less than 5%. No new pseudocontact shifts were observed for residues in site II. This indicates nonrandom filling in sites II and sites I. Such observations indicate that up to a M/P ratio of 3:1, Tm^{3+} binds mostly to the N-terminal domain and preferentially to site II, followed by site I. During the course of titration, the integral volumes of pseudocontact-shifted cross-peaks of residues in site IV decrease marginally (~10%).

La^{3+} Titration of $(Ca^{2+})_4$-EhCaBP. We carried out Ca^{2+}-displacement by the diamagnetic lanthanum (La^{3+}) ion up to a M/P ratio of 1:1. The changes in the HSQC spectrum (Figure 6) due to minor structural changes caused by the La^{3+} also manifest themselves as changes in chemical shifts. These changes are observed only in the close vicinity of the calcium-binding loop in site III (spheres in Figure 4C), confined to within a radius of about 5 Å from the metal (The diamagnetic shifts of the unisubstituted La^{3+} species are provided in the Supporting Information). The chemical shift changes for the residues in the neighboring binding loop of the C-terminal domain and in the N-terminal domain were found to be negligibly small, indicating no major structural change (See Figure 7). The extent of changes observed in the chemical shifts of $^{1}H^{N}$ and ^{15}N spins are found to be smaller than those observed in calbindin D_{9K} (*14*) and could be attributed to the relatively more open conformation of the third Ca^{2+} binding loop in *Eh*CaBP compared to those observed in calcium binding loops of other proteins (*12*, *18*). Further the 3D [^{15}N-^{1}H] HSQC−NOESY recorded on (Ca^{2+})(I)-(Ca^{2+})(II)-(Yb^{3+})(III)-(Ca^{2+})(IV)-*Eh*CaBP provided almost the same set of NOE constraints for both the domains and in the linker region as in the case of $(Ca^{2+})_4$-*Eh*CaBP. The observed variations in the distance constraints derived using CALIBA (*31*) (see Supporting Information, Figure S2) for the N-terminal domain and the linker region were found to be within 0.05 Å. In the case of the C-terminal domain, the residues in the fourth site show small differences in the derived distance constraints (average variation of 0.15 Å), while for residues in site III, the differences are around 0.2−0.8 Å. The close similarity in NOE constraints seen for the (Ca^{2+})(I)-(Ca^{2+})(II)-(Yb^{3+})(III)-(Ca^{2+})(IV)-*Eh*CaBP and $(Ca^{2+})_4$-*Eh*CaBP supports the fact that their 3D structures are almost identical.

Isothermal Calorimetry (ITC). In a two-metal (Ca^{2+}) binding site (N-terminal and C-terminal domain of *Eh*CaBP), the binding of the lanthanide to one site while the other one is occupied by Ca^{2+} is represented by the intrinsic association constants k_1 (for the first site) and k_2 (for the second). When one site is occupied, the binding of the second ion is then

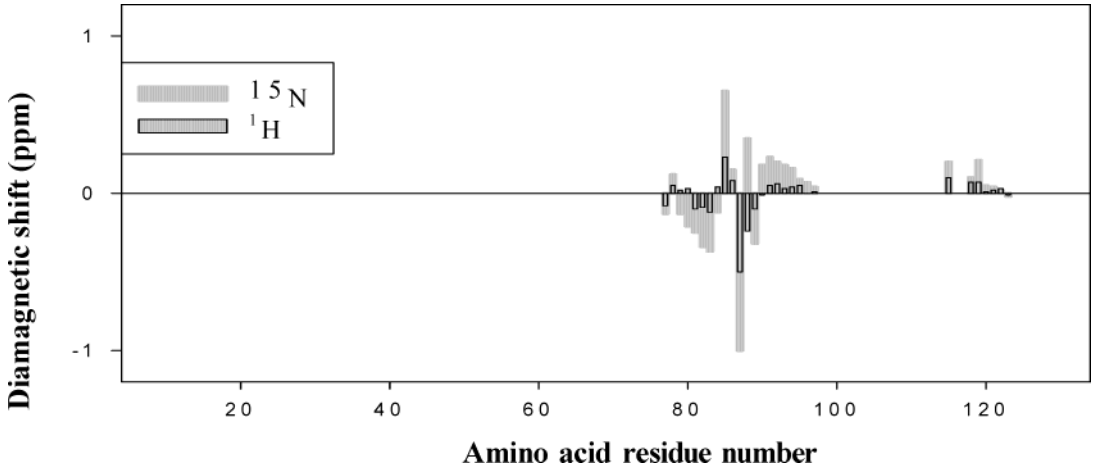

FIGURE 7: The histogram of differences in $^{15}N/^{1}H^{N}$ chemical shifts as noted from the 2D [^{15}N-^{1}H] HSQC spectra of $(La^{3+})(Ca^{2+})_3$-*Eh*CaBP and $(Ca^{2+})_4$-*Eh*CaBP for each amino acid residue.

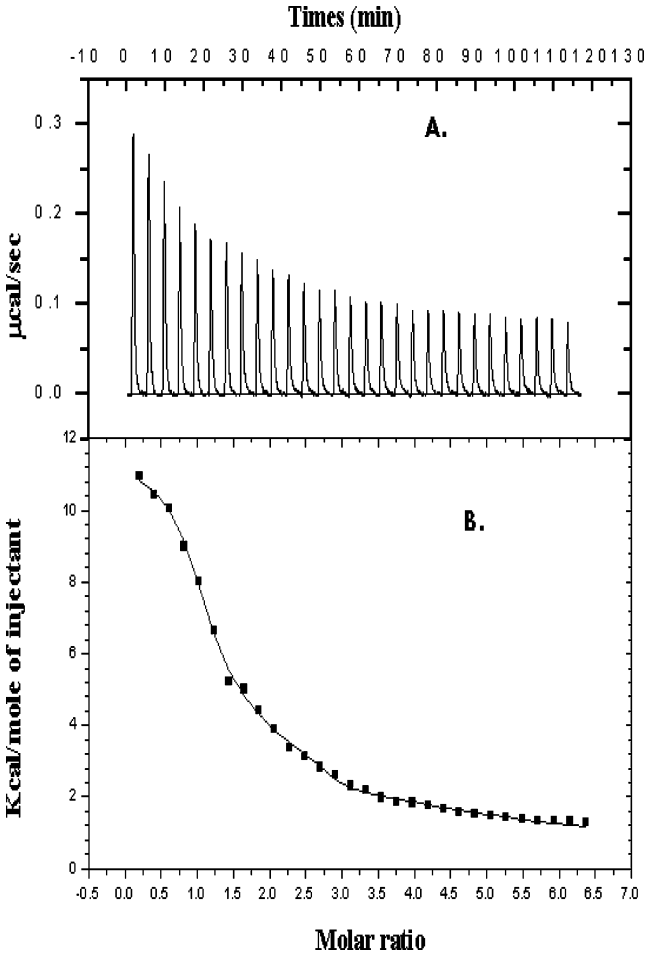

FIGURE 8: Calorimetric titration (A) of 4 μL aliquots of 7.5 mM $Tm^{3+}Cl_3$ solution into 0.11 mM Ca^{2+}-loaded *Eh*CaBP at 308 K and (B) plot of kilocalories per mole of heat absorbed or released per injection of $Tm^{3+}Cl_3$ as a function of metal/protein ratio at 308 K and the best least-squares fit of the data to binding models described in the text.

given by either $k_{2,1}$ or $k_{1,2}$. Thus, experimental analysis of the binding energetics for a two-site system demands at least three ($2^n - 1$; where n is the number of binding sites) independent observables. In the case that the values of the microscopic binding constants k_1 and k_2 for the two sites under consideration are widely different, the protein will exhibit a stepwise (sequential) metal binding. For example, if k_1 is much larger than k_2, then for a given molecule in an ensemble the probability of ligand binding to the first site (k_1) followed by the second ($k_{2,1}$) is significantly high, having three possibilities, such as, (i) $k_1 = k_{2,1}$, which results in equal populations of only the first site filled (say *A*) and both the sites filled (say *B*), (ii) $k_1 > k_{2,1}$, which results in $A > B$, and (iii) $k_1 < k_{2,1}$, which results in $A < B$. In all such situations, NMR measurements not only provide the site-specific information, owing to the most probable microscopic pathway in binding, but also the populations of respective species. From such insight into the microscopic binding pathway, one can then correlate the macroscopic binding constants derived from ITC measurements with the microscopic counterparts. However, if the binding is not sequential, we have a complex binding scheme. For a four site system, we need 15 ($2^n - 1$) observables to describe the binding or displacement process.

The calorimetric reaction of the addition of Tm^{3+} to *Eh*CaBP is shown in Figure 8A, while the heat exchanged, ΔQ, vs the M/P ratio is shown in Figure 8B. By variation of the initial parameters of the fitting procedure, it is found that the fit is stable for a macroscopic four-site sequential displacement scheme (*26*) and no other parameter set can fit the data better. The curve fitting reveals the endothermic nature of the Ca^{2+} displacement by Tm^{3+}. The endothermic nature of Ca^{2+} displacement is obvious considering the fact that the hydration enthalpy of Tm^{3+} is higher than that of Ca^{2+} (*32*). This implies that the energy released upon Ca^{2+} hydration is not sufficient to break the Tm^{3+} hydration shell, resulting in heat being absorbed from the solution. It may be noted that the sequential displacement scheme used to fit ITC data is macroscopic, bearing no site-specific information. It is NMR that provides the site-specific information on displacement, and combination of ITC and NMR completely describes the whole displacement process. The sequential nature and the order of Ca^{2+} displacement (site III first, followed by sites II, I, and IV) by Tm^{3+} are found to be similar to those of Yb^{3+}. An additional observation, however, in the Tm^{3+} titration is the observation of interdomain pseudocontact shifts and an insight into intradomain and interdomain cooperativity.

Energetics Derived from ITC Titration and Functional Relationship between Macroscopic and Microscopic Rate Constants. Because the binding of the four Tm^{3+} ions to *Eh*CaBP is sequential, the ITC data can be analyzed in terms of four macroscopic binding constants, K_1, K_2, K_3, and K_4. These constants, together with the associated thermodynamic parameters, are listed in Table 1.

$$\mathrm{CaBP} + \mathrm{Tm}^{3+} \rightarrow \mathrm{CaBP(Tm}^{3+}); \quad K_1 = \frac{[\mathrm{CaBP(Tm}^{3+})]}{[\mathrm{CaBP}][\mathrm{Tm}^{3+}]}$$

$$\mathrm{CaBP(Tm}^{3+}) + \mathrm{Tm}^{3+} \rightarrow \mathrm{CaBP(Tm}^{3+})_2; \quad K_2 = \frac{[\mathrm{CaBP(Tm}^{3+})_2]}{[\mathrm{CaBP(Tm}^{3+})][\mathrm{Tm}^{3+}]}$$

$$\mathrm{CaBP(Tm}^{3+})_2 + \mathrm{Tm}^{3+} \rightarrow \mathrm{CaBP(Tm}^{3+})_3; \quad K_3 = \frac{[\mathrm{CaBP(Tm}^{3+})_3]}{[\mathrm{CaBP(Tm}^{3+})_2][\mathrm{Tm}^{3+}]}$$

$$\mathrm{CaBP(Tm}^{3+})_3 + \mathrm{Tm}^{3+} \rightarrow \mathrm{CaBP(Tm}^{3+})_4; \quad K_4 = \frac{[\mathrm{CaBP(Tm}^{3+})_4]}{[\mathrm{CaBP(Tm}^{3+})_3][\mathrm{Tm}^{3+}]}$$

The equilibrium concentrations of all the species involved can be expressed as a function of $[Tm^{3+}]$ as

$$[\mathrm{CaBP}] = C_{\mathrm{CaBP}}/\{1 + K_1[\mathrm{Tm}^{3+}] + K_1K_2[\mathrm{Tm}^{3+}]^2 + K_1K_2K_3[\mathrm{Tm}^{3+}]^3 + K_1K_2K_3K_4[\mathrm{Tm}^{3+}]^4\} \quad \text{(A)}$$

$$[\mathrm{CaBP(Tm}^{3+})] = K_1[\mathrm{CaBP}][\mathrm{Tm}^{3+}] \quad \text{(B)}$$

$$[\mathrm{CaBP(Tm}^{3+})_2] = K_2[\mathrm{CaBP(Tm}^{3+})][\mathrm{Tm}^{3+}] \quad \text{(C)}$$

$$[\mathrm{CaBP(Tm}^{3+})_3] = K_3[\mathrm{CaBP(Tm}^{3+})_2][\mathrm{Tm}^{3+}] \quad \text{(D)}$$

$$[\mathrm{CaBP(Tm}^{3+})_4] = K_4[\mathrm{CaBP(Tm}^{3+})_3][\mathrm{Tm}^{3+}] \quad \text{(E)}$$

where C_{CaBP} is the total protein concentration. In these

Table 1: The ITC Results for Tm^{3+}Displacement

macroscopic rate constant	value of macroscopic rate constant (M^{-1})	Gibbs free energy, ΔG (kJ/mol)	enthalpy, ΔH (kJ/mol)	entropy, $T\Delta S$ (kJ/mol)	microscopic binding constant	binding constants from simulation using sequential model (M^{-1})
K_1	$(1.84 \pm 0.015) \times 10^6$	−36.483	45.654 ± 0.285	82.137	k_{III}	1.84×10^6
K_2	$(1.25 \pm 0.012) \times 10^5$	−29.788	22.739 ± 0.190	52.527	$k_{II,III}$	1.25×10^5
K_3	$(1.02 \pm 0.01) \times 10^5$	−29.374	6.416 ± 0.116	35.790	$k_{I,II,III}$	1.02×10^5
K_4	$(3.94 \pm 0.026) \times 10^2$	−14.433	80.966 ± 1.049	95.399	$k_{IV,I,II,III}$	394

Table 2: ITC Results for Yb^{3+} Displacements

macroscopic binding constant	value of macroscopic binding constant (M^{-1})	enthalpy, ΔH (kJ/mol)	Gibbs free energy, ΔG (kJ/mol)	entropy, $T\Delta S$ (kJ/mol)	microscopic binding constants	binding constants from sequential model (M^{-1})
K_3	$(1.55 \pm 0.45) \times 10^4$	188.7 ± 87.6	−25.88	214.6	$k_{I,II,III}$	1.85×10^4
K_2	$(2.46 \pm 1.40) \times 10^4$	117.1 ± 10.4	−24.69	141.8	$k_{II,III}$	2.26×10^4
K_1	$(1.25 \pm 0.38) \times 10^5$	41.8 ± 1.1	−30.04	71.8	k_{III}	1.55×10^5
K_4	$(1.78 \pm 1.20) \times 10^3$	−210.5 ± 96.2	−19.16	−191.3	$k_{IV,I,II,III}$	1.78×10^3

calculations, the concentration of free Ca^{2+} was assumed constant throughout the titration because the initial Ca^{2+} concentration in the sample was kept much higher than the protein concentration. The NMR data reveals Ca^{2+}displacement first from site III followed by sites II, I, and IV. During the course of such displacement, no evidence of parallel displacement from any pair of sites is observed. During the initial stages of titration, the macroscopic unisubstituted lanthanide species CaBP(Tm^{3+}) is composed of only one major microscopic species (Ca^{2+})(I)-(Ca^{2+})(II)-(Tm^{3+})(III)-(Ca^{2+})(IV)-*Eh*CaBP), resulting from Ca^{2+} displacement from site III alone. Hence, the first macroscopic binding constant (K_1), measured by ITC turns out to be the microscopic (site-specific) binding constant k_{III}. Similarly, the unisubstituted CaBP(Tm^{3+}) species are then transformed by the next incoming Tm^{3+} into CaBP(Tm^{3+})$_2$ species with Ca^{2+} displacement mainly from site II. This enables one to assign $k_{II,III} = (K_2)$. Further, the rest of the sequential displacement process revealed by NMR data helps in concluding that $k_{I,II,III} = K_3$ and $k_{IV,I,II,III} = K_4$.

Comparison of Energetics of Ca^{2+} Displacement by Tm^{3+} and Yb^{3+}. The binding constants, enthalpies, and entropies for the four metal binding sites for Tm^{3+} and Yb^{3+} are given in Tables 1 and 2, respectively. The results show that binding constants for sites III, II, and I in Tm^{3+} are an order of magnitude greater than those of Yb^{3+} but that of the fourth site is 5 times smaller. Such differences can be attributed to the small difference in ionic radii and hydration energy (*32*, *33*). As mentioned earlier, we could not carry out Tm^{3+} titration experiments beyond a M/P ratio of 3.0. To have an estimate of the Ca^{2+} displacement beyond the M/P ratio of 3.0, we extrapolated the simulated curves and found that the Ca^{2+} in the 4th site is displaced to an extent of only 30% at a M/P ratio of 4.0 as compared to 65% in case of Yb^{3+} for the same M/P ratio (see Supporting Information, Figure S3). This reveals high specificity of site IV for Ca^{2+}.

Interdomain Cooperativity. NMR and ITC data taken together clearly establish the existence of interdomain cooperativity in *Eh*CaBP. The fact that no PCSs are seen for residues in site III (during the initial course of titration) shows that parallel displacement from sites II and IV is negligible. It may be recalled that site I does not show any decrease in integral volumes of cross-peaks belonging to their residues during the initial stages of titration (Tm^{3+}/protein ratio if changed from 0:1 to 1:1). This also excludes parallel filling between sites III and I.

In a microscopic point of view Tm^{3+} displaces Ca^{2+} first from site III, primarily because of its open loop conformation and the presence of three aspartate residues at X, Y, and Z positions of the metal binding loop (*12*, *18*). Once site III is saturated with Tm^{3+}, the next incoming Tm^{3+} displaces Ca^{2+} from site II, having two aspartate residues at X and Y positions. Cooperativity between sites III and II in *Eh*CaBP can be characterized by $\Delta\Delta G$, which quantifies the increase or decrease in the free energy of one of the sites upon Ca^{2+} displacement by Tm^{3+} in the neighboring site (*34*−*36*).

$$\Delta\Delta G = \Delta G_{II,III} - \Delta G_{II} = -RT \ln(k_{II,III}/k_{II})$$

To have sequential displacement between sites III and II, the intrinsic displacement affinity of site II (k_{II}) must be at least 10^2 times lower than that ofsite III (k_{III}), of which the intrinsic displacement affinity is on the order of 10^6 M^{-1} (K_1). If the displacement affinity were less than 100 times smaller, pseudocontact-shifted peaks from site III caused by Tm^{3+} binding to site II would have been observed with >1% intensity, which is our estimated detection limit. However, when site III is already filled, the probability of Ca^{2+} displacement by the incoming Tm^{3+} increases in site II, resulting in a value of $k_{II,III} \approx 10^5$ M^{-1} (assigned equal to macroscopic rate constant K_2). Hence, the ratio $k_{II,III}/k_{II} >$ 10 results in the value of $-\Delta\Delta G$ being positive, indicating positive interdomain cooperativity between them (sites II and III).

Such an interdomain cooperativity could not be established earlier by following Ca^{2+} displacement by Yb^{3+} owing to the weak ligand field of Yb^{3+} (*18*). Hence the two domains were considered to be independent, and the description of the sequential displacement was restricted to individual domains. A question that arises is whether interdomain cooperative interaction is linked to any structural changes that may occur due to the trivalent Ln^{3+} ion displacing the divalent Ca^{2+} ion. We have carried out an independent experiment of Ca^{2+} displacement by a diamagnetic La^{3+}. Minor structural changes, reflected as changes in chemical shifts only in the close vicinity of the calcium binding loop (Figure 7), reveal that the origin of cooperativity and

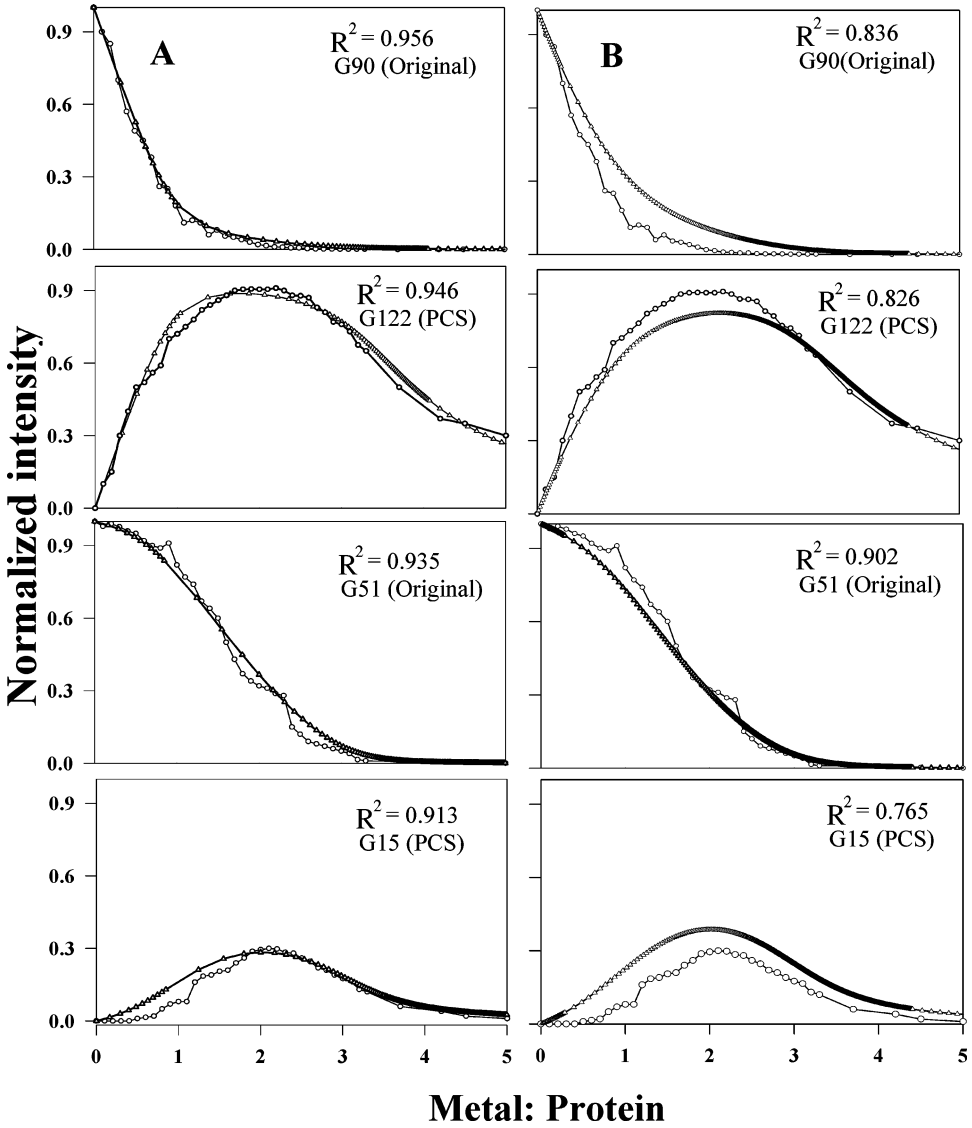

FIGURE 9: Superposition of experimental and simulated plots of intensity profiles of the original and pseudocontact-shifted cross-peaks of G15 and G122 during the Yb^{3+} titration by considering the (A) sequential filling model and (B) domain-independent model: (●) simulated and (△) experimental curves. The thermodynamic constants used in simulations are listed in Table 2. The corresponding R^2 values are given at the upper-right corner of the respective plots.

sequential displacement are primarily due to the intrinsic specificities of individual sites, dictated by the composition of the amino acid residues in the loop, the difference in charge, or both, rather than the structural changes.

Intradomain Cooperativity. Like the interdomain cooperativity, the NMR and ITC data taken together also shed light on intradomain cooperativity in the Ca^{2+} displacement process in *Eh*CaBP. It may be recalled that the pair of EF-hands within a Ca^{2+} binding domain are highly cooperative in Ca^{2+} binding. Once Ca^{2+} is completely displaced from site III, the next displacement is from site II, followed by site I. As in the case of interdomain cooperativity, the intradomain cooperativity between sites II and I in *Eh*CaBP can be characterized by $\Delta\Delta G$, which quantifies the increase or decrease in the free energy of one of the sites upon Ca^{2+} displacement by Tm^{3+} in the neighboring site (*34*−*36*).

$$\Delta\Delta G = \Delta G_{I,II,III} - \Delta G_{I,III} = -RT \ln(k_{I,II,III}/k_{I,III})$$

Now, to have sequential displacement between sites I and II when site III is already filled, the intrinsic displacement affinity of site I ($k_{I,III}$) must be at least $>10^2$ times lower than that of site II ($k_{II,III}$), of which the intrinsic displacement affinity is on the order of 10^5 M^{-1} (K_2). However, when the sites III and II are already filled the probability of Ca^{2+} displacement by the incoming Ln^{3+} increases in site I, resulting in a value of $k_{I,II,III} \approx 10^5$ M^{-1} (assigned equal to macroscopic rate constant K_3). Hence, the lower limit of 100 for the $k_{I,II,III}/k_{I,III}$ ratio results in the value of $-\Delta\Delta G$ being positive, indicating that the intradomain cooperativity between sites I and II is also positive. Since the structural changes are mainly confined to the calcium binding loop where the lanthanide is bound, the intradomain cooperativity between sites I and II must not be due to induced structural changes. The intradomain cooperativity between sites II and I is identical to the observations made earlier during the course of Yb^{3+} titration of *Eh*CaBP (*18*).

Simulations. The changes in the observed integral volumes for original peaks of G15 and G90 and pseudocontact-shifted peaks of G15, G51, and G122 (Figure 3A) as a function of the M/P ratio are simulated using the macroscopic displacement equations mentioned above (eqs A, B, C, D, and E)

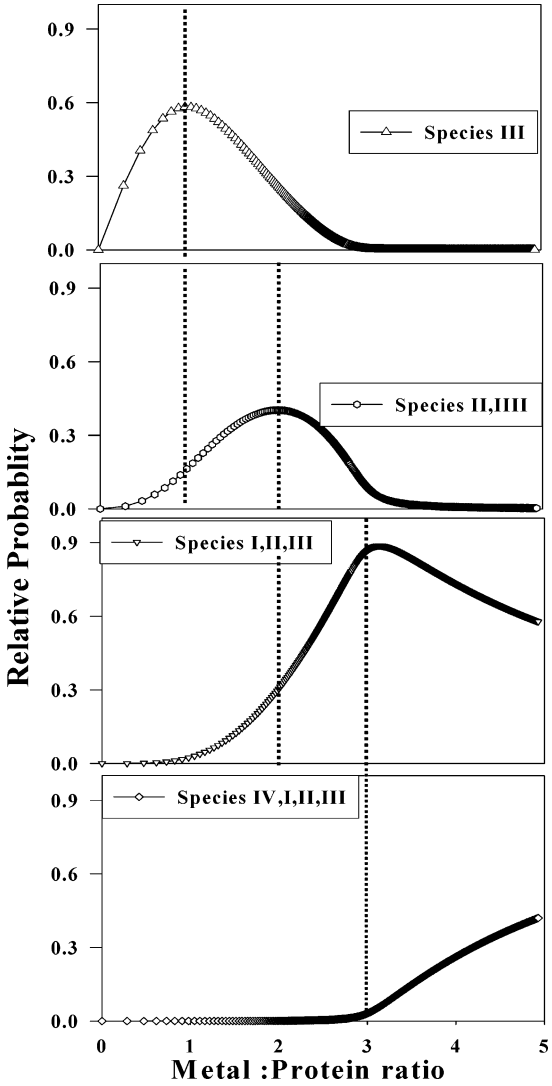

FIGURE 10: The computed probability of having one, two, three, and four sites occupied by Tm^{3+} as a function of the Tm^{3+}/protein ratio using the site-specific (microscopic) sequential pathway inferred from NMR data and correlating the microscopic displacement constants with the macroscopic counterparts derived from ITC data (Table 1).

and assigning the macroscopic binding constants to their microscopic counterparts on the basis of NMR data (site-specific sequential model), and excellent fits could be obtained (Figure 3A) with comparably good R^2 values (shown in as insets of Figure 3A). Thus, the sequential displacement model correctly assigns all microscopic binding constants with their corresponding macroscopic counterparts derived from ITC data. However, in the case of Yb^{3+} titration, when the simulations are carried out with a domain-independent model (displacements of Ca^{2+} in each domain are considered to be independent of each other, see equations in the supplementary material of Atreya et al. (*18*)) using the experimental values from ITC (Figure 9B), the fit is not perfect, as is evident from the poor R^2 values (shown in as insets of Figure 9B). This is primarily because, during the initial stages of titration, unisubstituted Yb^{3+} species would be either site II ((Ca^{2+})(I)-(Yb^{3+})(II)-(Ca^{2+})(III)-(Ca^{2+})(IV)-*Eh*CaBP) or site III ((Ca^{2+})(I)-(Ca^{2+})(II)-(Yb^{3+})(III)-(Ca^{2+})-(IV)-*Eh*CaBP) filled, and both species will sum up to give the macroscopic CaBP(Yb^{3+}) species mentioned above. Thus, the contribution to K_1 would come from both k_{III} and k_{II}.

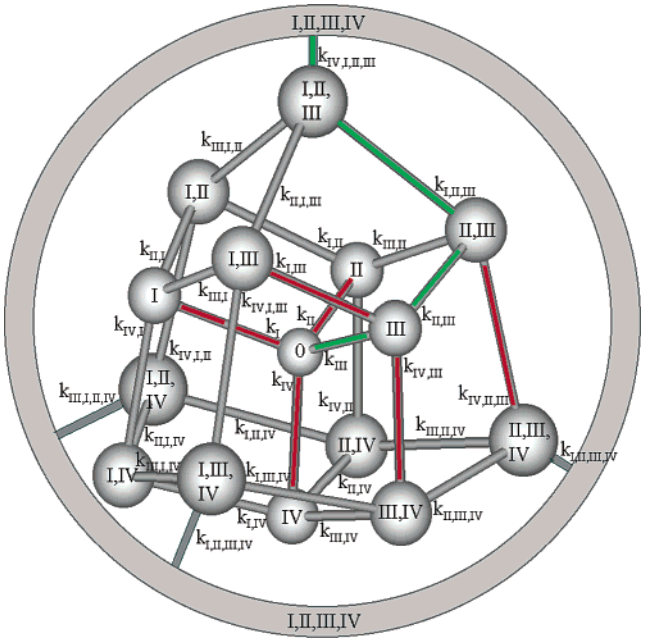

FIGURE 11: Graphical representation of the 16 species and the 32 equilibria among them in $(Ca)_n(Ln)_{4-n}$-*Eh*CaBP ($n = 0-4$). Starting from the $(Ca)_4$-*Eh*CaBP species (species 0), the filling pathway upon titration with Ln^{3+} up to $(Ln)_4$-*Eh*CaBP (species I,II,III,IV) is indicated in green, and the several possible branchings along the pathway that can be ruled out by NMR data are indicated in red.

Hence, assigning K_1 for k_{III} would be incorrect (see Appendix I for discussion of domain-independent and sequential models for a two-domain four-site calcium binding protein). This is also evident from the fact that using a domain-independent model the match was perfect only if k_{III} was set equal to $3K_1$ (*18*). On the other hand, if Ca^{2+} displacement by Yb^{3+} is assumed to be sequential, the experimental and simulated curves fit perfectly within the experimental error limit (Figure 9A) with comparably very good R^2 values. Thus, in the case of Yb^{3+} too, the sequential displacement model correctly assigns all microscopic binding constants with their corresponding macroscopic counterparts derived from ITC data with very good R^2 values (shown in as insets of Figure 9A). Further, in the case of Tm^{3+} titration, when the simulations are carried out with a domain-independent model using the experimental ITC values (Figure 3B), the fits are expectedly imperfect (the corresponding R^2 values are shown in as insets of Figure 3B). Further, to validate the sequential model of Ca^{2+} displacement by Tm^{3+} proposed here, we have calculated the probability of having one, two, three and four sites occupied by Tm^{3+} as a function of the Tm^{3+}/protein ratio using the site-specific (microscopic) sequential pathway inferred from NMR data and correlating the microscopic displacement constants with the macroscopic counterparts derived from ITC data (Table 1). The Figure 10, thus obtained, supports site-specific sequential Ca^{2+} displacement revealed by NMR data, first from site III and then followed by displacements from sites II and I. Ca^{2+} is finally displaced from site IV only to an extent of 70% of the original population at an M/P ratio of 4. Figure 11 shows graphical representation of the 16 species and the 32 equilibria among them in $(Ca)_n(Ln)_{4-n}$-*Eh*CaBP ($n = 0-4$). Starting from the $(Ca)_4$-*Eh*CaBP species (species 0), the displacement pathway upon titration with Ln^{3+} up to $(Ln)_4$-*Eh*CaBP (species I,II,III,IV) is indicated in green, and several other possible

branchings along the pathway that can be ruled out by NMR data are indicated in red. Despite the potential complexity of the equilibria involved, the present NMR data has demonstrated that the only significant pathway for lanthanide binding (in green) goes from 0 to III (avoiding other possibilities 0 to I, 0 to II, and 0 to IV in red), then proceeds to II,III (avoiding branching to I,III and IV,III), and finally to I,II,III (avoiding branching to (IV,II,III). Site IV is finally filled starting from I,II,III (shown as a circle).

CONCLUSIONS

This study provides a basis for understanding the behavior of lanthanides when used as a substitute for Ca^{2+}, the pattern of sequential binding, the structural change involved, the range and magnitude of paramagnetic interactions, and associated energetics. The cooperativity in the lanthanide-for-calcium substitution has a different meaning with respect to cooperativity in metal binding to the apo-protein. In the latter case, calcium-sensor proteins undergo sizable conformational rearrangements in response to calcium binding, and therefore, the conformational change plays an important role in the overall energetics (*37*). In contrast, in metal substitution the structure of the holo-protein is essentially maintained, and what one measures is the differential metal binding contribution to the energy. The novel finding of positive interdomain cooperativity is particularly interesting, because it points to some kind of domain−domain interaction the contribution of which to the energetics of the whole process must be metal-dependent.

The present study also provides a background for a better theoretical understanding of the cooperativity and PCS shifts. The assigned values of PCSs could be used as structural constraints to refine the description of the solution structure of this two-domain protein. This work will be reported elsewhere.

ACKNOWLEDGMENT

The facilities provided by the National Facility for High Field NMR, supported by Department of Science and Technology (DST), Department of Biotechnology (DBT), Council of Scientific and Industrial Research (CSIR), and Tata Institute of Fundamental Research, Mumbai, India, are gratefully acknowledged. We thank Prof. Alok Bhattacharya (JNU, New Delhi) for providing the *Eh*CaBP clone, Dr. H. S. Atreya for recording some of the 2D NMR spectra, and Prof. Girjesh Govil for his critical comments.

SUPPORTING INFORMATION AVAILABLE

The list of ^{15}N-^{1}H PCS shifts for Tm^{3+} and Yb^{3+} substituted species obtained from 2D [^{15}N-^{1}H] HSQC spectra; the diamagnetic shifts in $(La^{3+})(Ca)_3$-*Eh*CaBP; the list of $^{13}C'$, $^{13}C^{\alpha}$, and $^{13}C^{\beta}$ PCS shifts for unisubstituted Tm^{3+} species obtained from 3D NMR spectra; all the NOE constraints obtained from 3D [^{15}N-^{1}H] HSQC−NOESY spectra of $[Yb^{3+}][Ca^{2+}]_3$-*Eh*CaBP; the histogram of differences in $^{15}N/^{1}H^{N}$ chemical shifts for each amino acid residue, as noted from the 2D [^{15}N-^{1}H] HSQC spectra of $(La^{3+})(Ca^{2+})_3$-*Eh*CaBP and $(Ca^{2+})_4$-*Eh*CaBP and an analogous calcium binding protein ($(La^{3+})(Ca^{2+})$-calbindin D_{9K} and $(Ca^{2+})_2$-calbindin D_{9K}; the average variation of NOE constraints and extrapolated curves of NMR cross-peaks of Tm^{3+} titration; the histogram figure showing the range of PCS shifts in unisubstituted Yb^{3+} and Tm^{3+}. This material is available free of charge via the Internet at http://pubs.acs.org.

APPENDIX I. SEQUENTIAL AND DOMAIN-INDEPENDENT MODELS IN A TWO-DOMAIN FOUR-SITE CALCIUM BINDING PROTEIN

The macroscopic binding constants derived from the ITC measurements represent bulk property of the system. Even in the case of two-site system, if the binding is not sequential, we end up having a complex binding scheme. A simple theoretical model for the metal binding can provide a functional relationship between macroscopic and microscopic rate constants, which is discussed in detail, in the following paragraphs.

Sequential Ca^{2+} Displacement by Ln^{3+} Where the Two Domains Are Not Considered Independent. Considering the displacement reaction in a two-domain four-site system, such as *Eh*CaBP, we need 15 ($2^n - 1$) observables to describe the binding or displacement process. These observables can be represented by (i_1, i_2, i_3, i_4), where i_1, i_2, i_3, and i_4 take binary numbers, 0 for the presence of Ca^{2+}, 1 for the presence of Ln^{3+}, and they represent essentially the state of the four sites. For example, (0, 0, 1, 0) represents the (Ca^{2+})(I)-(Ca^{2+})(II)-(Ln^{3+})(III)-(Ca^{2+})(IV)-*Eh*CaBP species, while (0, 1, 1, 0) represents (Ca^{2+})(I)-(Ln^{3+})(II)-(Ln^{3+})(III)-(Ca^{2+})-(IV)-*Eh*CaBP, and so on and so forth. In such a situation, the experimental analysis of the energetics becomes very complex. However, if the binding/displacement process is sequential, the system becomes amenable for description with just four macroscopic binding constants. The sequential nature and the order of Ca^{2+} displacement (site III first, followed by sites II, I, and IV) by Tm^{3+} discussed above is a unique case. And in such a displacement reaction, species such as (1000), (0100), (1100), (1010), (0001), (1001), (0101), (1101), (0011), (1011), and (0111) are not present at all and hence are not observable. Thus, considering the sequential model, microscopically the reaction follows the following pathway:

$$(0000) \xrightarrow{k_{III}} (0010) \xrightarrow{k_{II,III}} (0110) \xrightarrow{k_{I,II,III}} (1110) \xrightarrow{k_{IV,I,II,III}} (1111)$$

The first step (0000) → (0010) is the equivalent of the macroscopic equation

$$CaBP + Ln^{3+} \rightarrow CaBP(Ln^{3+}); \quad K_1 = \frac{[CaBP(Ln^{3+})]}{[CaBP][Ln^{3+}]}$$

Since there is no parallel filling in any other sites, the macroscopic unisubstituted species $CaBP(Ln^{3+})$ has its only contribution from the microscopic species (0010). Hence, $K_1 = k_{III}$, since k_{III} is the only microscopic rate constant that contributes to the growth of macroscopic unisubstituted species $CaBP(Ln^{3+})$ by increasing the microscopic species (0010). Similarly, we can assign $k_{II,III} = K_2$, $k_{I,II,III} = K_3$, and $k_{IV,I,II,III} = K_4$ with clarity. The macroscopic sequential binding scheme used in fitting the ITC data (*26*) described above is macroscopic in nature dealing with macroscopic binding constants; it does not have any site-specific information. Even though such a macroscopic scheme is sequential,

there may be a large number of microscopic pathways in the displacement reaction including parallel ones that the system might undergo in attaining saturation. For example, the contributions of macroscopic species CaBP(Ln^{3+}) can come from four possible microscopic species (0010), (0100), (1000), and (0001). However, the sequential model from NMR data helps us to conclude that only the (0010) species contributes to CaBP(Ln^{3+}). So in the present case, the sequential model has helped us to sort out the most probable microscopic pathway in attaining saturation, making it microscopic in the true sense.

Domain-Independent Ca^{2+} Displacement by Ln^{3+}: For the same two-domain four-site system discussed above in which the displacement is sequential but independent between the two domains (as illustrated in the supplementary material in Atreya. et al. (*18*)), the rate [these are not rates, just microscopic thermodynamic constants] equations for the N-terminal domain, where the second site filling is followed by the filling of the first site, simplifies as

$$[Ca(I)][Ca(II)][CaBP] + Ln^{3+} \xrightarrow{k_{II}} [Ca(I)][Ln(II)][CaBP]$$

$$[Ca(I)][Ln(II)][CaBP] + Ln^{3+} \xrightarrow{k_{I,II}} [Ln(I)][Ln(II)][CaBP]$$

while for the C-terminal domain, where the third site filling is followed by the filling of the fourth site, they read as

$$[Ca(III)][Ca(IV)][CaBP] + Ln^{3+} \xrightarrow{k_{III}} [Ln(III)][Ca(IV)][CaBP]$$

$$[Ln(III)][Ca(IV)][CaBP] + Ln^{3+} \xrightarrow{k_{IV,III}} [Ln(III)][Ln(IV)][CaBP]$$

Thus, when Ln^{3+} goes to the 2nd site, whatever the condition of the C-terminal domain, the species undergoing second site (K_{II}) binding are the following:

$$(0000) \xrightarrow{k_{II}} (0100) \quad (1a)$$

$$(0010) \xrightarrow{k_{II}} (0110) \quad (1b)$$

$$(0011) \xrightarrow{k_{II}} (0111) \quad (1c)$$

and hence, this reaction follows three different possible pathways.

Similarly, if it were to be the third site binding (K_{III}) in C-terminal domain, whatever the condition of the N-terminal domain, we end-up having three possible reaction pathways such as,

$$(0000) \xrightarrow{k_{III}} (0010) \quad (2a)$$

$$(0100) \xrightarrow{k_{III}} (0110) \quad (2b)$$

$$(1100) \xrightarrow{k_{III}} (1110) \quad (2c)$$

Further, from eqs 1a and 2a, we have

$$(0000) \xrightarrow{k_{II}} (0100)$$

$$(0000) \xrightarrow{k_{III}} (0010)$$

which are essentially analogues to the macroscopic equation

$$[Ca]_4[CaBP] \xrightarrow{K_1} [Ca]_3[Ln][CaBP]$$

Hence, the contribution to K_1 will come from both k_{II} and k_{III}, because in such a situation there is parallel filling between sites II and III. Both species (0010) and (0100) contribute to CaBP(Ln^{3+}). So, assigning K_1 for k_{III} would be incorrect. Similarly, other assignments of macroscopic rate constants would have contributions from several other microscopic rate constants and are also incorrect.

REFERENCES

1. Christopher, D. H., Haque, R., and Petri, W. A., Jr. (1999) Molecular-based diagnosis of *Entamoeba Histolytica* infection, *Exp. Rev. Mol. Med. 22* (March).
2. Ravdin, J. I., Murphy, C. F., Guerrant, R. L., and Long- Kruz, S. A. (1985). Effect of antagonists of calcium and phospholipase A on the cytopathogenicity of *Entamoeba histolytica*, *J. Infect. Dis. 152, 542*−*549*.
3. Munoz, M. L., O'Shea-Alveraz, M. S., Perez-Garcio, J., Weinbach, E. C., Mereno, M. A., and Tovar, R. (1992) Purification and biochemical properties of calmodulin in *Entamoeba histolytica* and its distribution during secretion of electron-dense granules, *Comp. Biochem. Physiol. B103*, 517−521.
4. Carbajol, M. E., Manning-Cela, R., Pina, A., Frano, E., and Meza, I. (1996) Fibronectin-induced intracellular calcium rise in *Entamoeba histolytica* trophozoites: effect on adhesion and the actin cytoskeleton, *Exp. Parasitol. 82*, 11−20.
5. Prasad, J., Bhattacharya, S., and Bhattacharya, A., (1992) Cloning and sequence analysis of a calcium-binding protein gene from a pathogenic strain of *Entamoeba histolytica*, *Mol. Biochem. Parasitol. 52*, 137−140.
6. Linse, S., and Forsén, S. (1995) Determinants that govern high-affinity calcium binding, *Adv. Second Messenger Phosphoprotein Res. 30*, 89−151.
7. Kretsinger, R. H., and Nockolds, C. E. (1973) Carp muscle calcium-binding protein. II. Structure determination and general description, *J. Biol. Chem. 248*, 3313−3326.
8. Nelson, M. R., and Chazin, W. J. (1998) Structures of EF-hand Ca^{2+}-binding proteins: Diversity in the organization, packing and response to Ca^{2+} Binding, *BioMetals 11*, 297−318.
9. Strynadka, N. C., and James, M. N. G. (1989) Crystal Structures Of The Helix-Loop-Helix Calcium-Binding Proteins, *Annu. Rev. Biochem. 58*, 951−958.
10. Lewit-Bentley, A., and Réty, S. (2000) EF-hand calcium-binding proteins, *Curr. Opin. Struct. Biol. 10*, 637−643.
11. Falke, J. J., Drake, S. K., Hazard, A. L., and Peersen, O. B. (1994) Molecular tuning of ion binding to calcium signaling proteins, *Q. Rev. Biophys. 27*, 219−290.
12. Atreya, H. S, Sahu, S. C., Bhattacharya, A., Chary, K. V. R., and Govil, G. (2001) NMR derived solution structure of an EF-hand calcium binding protein from *Entamoeba Histolytica*, *Biochemistry 40*, 14392−14403.
13. Shannon, R. D. (1976) Revised effective ionic radii in halides and chalcogenides, *Acta Crystallogr. A32*, 751−767.
14. Bertini, I., Janik, M. B., Lee, Y. M., Luchinat, C., and Rosato, A. (2001) Magnetic susceptibility tensor anisotropies for a lanthanide ion series in a fixed protein matrix, *J. Am. Chem. Soc. 123*, 4181−4188.
15. Allegrozzi, M., Bertini, I., Janik, M. B. L., Lee, Y. M., Liu, G., and Luchinat, C. (2000) Lanthanide induced pseudocontact shifts for the solution refinement of macromolecules in shells up to 40 A from the metal ion, *J. Am. Chem. Soc. 122*, 4154−4161.
16. Bertini, I., Janik, M. B. L., Liu, G., Luchinat, C., and Rosato, A. (2001) Crystal Structures of The Helix-Loop-Helix Calcium-Binding Proteins, *J. Magn. Reson. 148*, 23−30.
17. BieKofsky, R. R., Muskett, F. W., Schmitt, J. M., Martin, S. R., Browne, J. P., Bayley, P. M., and Feeney, J. (1999) NMR approaches for monitoring domain orientations in calcium-binding proteins in solution using partial replacement of Ca^{2+} by Tb^3, *FEBS Lett. 460*, 519−526.
18. Atreya, H. S., Mukherjee, S., Chary, K. V. R, Lee, Y. M., and Luchinat, C (2003) Structural basis for sequential displacement

of Ca^{2+} by Yb^{3+} in a protozoan EF-hand Calcium binding protein, *Protein Sci. 12*, 412−425.
19. Bertini, I., and Luchinat, C. (1996) NMR of paramagnetic substances, *Coord. Chem. Rev. 150*.
20. Sahu, S. C., Bhattacharya, A., Chary, K. V. R., and Govil, G. (1999) Secondary structure of a calcium binding protein (CaBP) from *Entamoeba*, *FEBS Lett. 459*, 51−56.
21. Kay, L. E., Keifer, P., and Saarinan, T. (1992) Pure absorption gradient enhanced heteronuclear single quantum correlation spectroscopy with improved sensitivity, *J. Am. Chem. Soc. 114*, 10663−10665.
22. Kay, L. E., Ikura, M., Tschudin, R., and Bax, A. (1990) Three-dimensional NMR spectroscopy of isotopically enriched proteins, *J. Magn. Reson. 89*, 496−514.
23. Grzesiek, S., and Bax, A. (1992) Correlating backbone amide and side chain resonances in larger proteins by multiple relayed triple resonance NMR, *J. Am. Chem. Soc. 114*, 6291−6293.
24. Grzesie, S., and Bax A. (1992) An efficient experiment from sequential backbone assignment of medium-sized isotopically enriched proteins, *J. Magn. Reson. 99*, 201−207.
25. Clubb, R. T., Thanabal, V., and Wagner, G. (1992) A Constant-Time Three-Dimensional Triple-Resonance Pulse Scheme to Correlate Intraresidue $^{1}H^{N}$, ^{15}N and $^{13}C'$Chemical Shifts in ^{15}N-^{13}C-Labeled Proteins, *J. Magn. Reson. 97*, 213−217.
26. Wiseman, T., Williston, S., Brandts, J. F., and Lin, L. N. (1989) Rapid measurement of binding constants and heats of binding using a new titration calorimeter, *Anal. Biochem. 79*, 131−137.
27. Akerfeldt, K. S., Coyne, A. N., Wilk, R. R., Thulin, E., and Linse, S. (1996) Ca^{2+} binding stoichiometry of calbindin D28K as assessed by spectroscopic analysis of synthetic peptide fragments, *Biochemistry 35*, 3662−3669.
28. Atreya, H. S., and Chary, K. V. R. (2000) Amino acid selective unlabeling for residue specific NMR assignments in proteins, *Curr. Sci. 79*, 504−507.
29. Atreya, H. S., and Chary, K. V. R. (2001) Selective 'unlabeling' of amino acids in fractionally ^{13}C labeled proteins: An approach for stereospecific NMR assignments of CH_3 groups in Val and Leu residues, *J. Biomol. NMR 19*, 267−272.
30. Banci, L., Bertini, I., Gori Savellini, G., Romagnoli, A., Turano, P., Cremoni, M. A., Luchinat, C., and Gray, H. B (1997) Pseudocontact shifts as constraints for energy minimization and molecular dynamics calculations on solution structures of paramagnetic metalloproteins, *Proteins: Struct., Funct., Genet. 29*, 68−76.
31. Günter, P., Braun, W., and Wuthrich, K. (1991) Efficient computation of three-dimensional protein structures in solution from nuclear magnetic resonance data using the program DIANA and the supporting programs CALIBA, HABAS and GLOMSA, *J. Mol. Biol. 217* (3), 517−530.
32. Macrus, Y. (1985) *Ion Solvation*, John & Wiley Sons Ltd, Chichester, U.K.
33. Abragam, A., and Bleaney, B. (1970) *Electron Paramagnetic Resonance of Transition Ions*, Oxford, U.K.
34. Weber, R. E., Lykkeboe, G., and Johansen, K. (1975). Biochemical aspects of the adaptation of hemoglobin-oxygen affinity of eels to hypoxia, *Life Sci. 17*, 1345−1349.
35. Linse, S., Teleman, O., and Drakenberg, T. (1990) Ca^{2+} binding to calbindin D9k strongly affects backbone dynamics: measurements of exchange rates of individual amide protons using ^{1}H NMR, *Biochemistry 29*, 5925−5934.
36. Gopal, B., Swaminathan, C. P., Bhattacharya, S., Bhattacharya, A., Murthy, M. R. N., and Surolia, A. (1997) Thermodynamics of Metal Ion Binding and Denaturation of a Calcium binding Protein from *Entamoeba histolytica*, *Biochemistry 36* , 10910−10916.
37. Maler, L., Blankenship, J., Rance, M., and Chazin, W. J. (2000) Site−site communication in the EF-hand Ca^{2+}-binding protein calbindin D9k, *Nat. Struct. Biol. 7*, 245−250.

BI049657D